Experimental Study of Rotor-Stator Contact Cycles

Elijah Chipato, A.D. Shaw, M.I. Friswell, R.S. Crespo

PII: S0022-460X(21)00169-3
DOI: https://doi.org/10.1016/j.jsv.2021.116097
Reference: YJSVI 116097

To appear in: *Journal of Sound and Vibration*

Received date: 4 June 2020
Revised date: 10 March 2021
Accepted date: 19 March 2021

Please cite this article as: Elijah Chipato, A.D. Shaw, M.I. Friswell, R.S. Crespo, Experimental Study of Rotor-Stator Contact Cycles, *Journal of Sound and Vibration* (2021), doi: https://doi.org/10.1016/j.jsv.2021.116097

Experimental Study of Rotor-Stator Contact Cycles

Elijah Chipato, A D Shaw, M I Friswell, R S Crespo

College of Engineering, Swansea University Bay Campus, Fabian Way, Crymlyn Burrows, Swansea SA1 8EN, UK

Abstract

A rotor can contact a stator thereby inducing some very strong non-linearities that can result in a plethora of vibration phenomena. Synchronous motions, chaotic motion, backward whirl, forward whirl are some of the reported phenomena in the literature. This article presents an experimental approach based on a very flexible rotor rig designed with drill string dynamics in mind for rotordynamic experiments. A non-contact technique was used for data acquisition using a consumer-grade Go-Pro Hero 6 Black camera which captures a series of images(video) which are then post-processed using MATLAB's image processing toolbox to understand the nature of dynamics involved. A mathematical model of the experimental rig was used for comparison with the actual experiment to assess the effectiveness of the data acquisition procedure used and validity of the model. The model is able to a good extent to reproduce the behaviour of the test rig. The fundamental phenomena exhibited by the system is analysed and discussed based on bifurcation plots, spectral intensity plots and orbit plots visualised in both rotating and stationary frame.

Keywords: Nonlinear, Rotordynamics, Periodic contacts, Backward whirl, Video

---

1. Introduction

Rubbing between the rotor and the stator can be found in many applications of engineering ranging from drill strings in the oil and gas industry, aero engines and even magnetic bearings. In flexible drill strings the rotor stator contact problem is well known [1, 2] and can be detrimental to the drill sting system if the high amplitude backward whirl is excited. In aero engines contact can occur between blades and the casing this could have been excited by the fan blade off scenario. This increases the unbalance forcing in the system thereby resulting in a response that is higher than the available clearance. Some typical examples of the severity of this problem is the grounding of the entire fleet of the F35A due to the engine catching fire because of excessive rubbing between the turbine blade and the cowling. In addition, in 1973 the NTSB reported a case that one of the engine fan assemblies disintegrated during flight because of the interaction between fan blade tip and the fan casing [3]. In the oil and gas industry system shut-down as a result of rotor stator contact can result in considerable costs to the organisation as well as the economy. This therefore shows that the rotor stator contact problem needs to be understood so as to circumvent these and other costly problems. Other authors such as [4–10] have used numerical simulations in a bid to understand the rotor stator contact problem.

Torkhani *et al.* [11] used a dedicated experimental setup to consider partial, light and severe rubs. Accelerometers and proximity probes were used to measure shaft and casing vibrations. A model which relies on finite element (FE) modelling suitable for real rotating machinery was then used for comparison with the experimental results. It was observed that the model reproduced the behaviour of the actual test rig. Ma *et al.* [12] considered a single span rotor system with two discs when the rubbing was between a disc and an elastic rod. An FE model of the rotor was developed and also compared with the actual experiment which made use of eddy current transducers for data acquisition. The Coulomb friction model was used to simulate rotor stator frictional characteristics. The effect of the gap and the contact stiffness was also assessed. It was noted that as the gap/clearance is decreased complicated impact rebounds are observed. When the contact stiffness was decreased the amplitude of both vibration and normal rubbing force decreased and the rotor stator contact time increased. The contact stiffness was noted to have greater influence on system vibration responses at higher speeds. It was also noted that the increase in amplitude of 2x, (1/2)x and (1/3)x harmonics and the normal rubbing force are a distinguishable characteristic to diagnose the worsening of rubbing. In addition, Chu and Lu [13] used an experimental set-up of a rub impact multi disk rotor system and observed multiple harmonic components such as 2x, 3x, etc. The (1/2) fractional harmonic components such as (1/2)x, (3/2)x and the (1/3) fractional harmonic components such as (1/3)x and (2/3)x were observed as well. As the rub-impact was aggravated, the spectrum composition became complicated and chaotic motions were observed.

Wang *et al.* [14] investigated the response of a rotor on a test rig with sudden unbalance. It was shown that the sudden unbalance has an impact effect on the rotor and that the critical speed frequency was excited and was characterised by an increase in the transient response upon sudden mass loss. The impact factor was also noted to be high at the supercritical state showing that rotors operating above the critical speed are more sensitive to a sudden unbalance load. Rub impact between the rotor and constraint ring was also found to add a load path to absorb part of the unbalance loads and also to generate additional stiffness (stiffening effect) which has a significant influence on the response of the rotor through an increase of the resonance speed as well as expansion of the resonance region.

In other work, Chen [15] simulated the casing vibrations resulting from blade-casing rub by introducing a new rub model and then using an aero engine rotor stator rig that uses acceleration sensors for data acquisition to validate the new improved model. The simulation results were observed to agree with the experiment thus validating the new model. The improved model can simulate a number of rubbing conditions including single point, multi point, local part and complete cycle rubbing on the casing and rotor. It was noted that for single point rubbing on the casing, the casing vibration has obvious periodic impact characteristics and the impact frequency is the frequency of the blades passing the casing and the impact is modulated by the rotational frequency. The characteristics of two point rubbing on the casing with complete-cycle rubbing on the rotor appeared to be the same as that of single point rubbing.

Ma *et al.* [16] also explored a similar blade casing rub model for both single and four-blade rubbings. Amplitude amplification phenomena was observed when multiple frequencies of the rotational frequencies coincided with the conical and torsional natural frequencies of rotor system, natural frequencies of the casing and the bending frequencies of the blades. This was also validated by a finite element model of the rotor system. Ma *et al.* [17] also formulated a new rubbing model between the rotating blade and the casing, where the model considered bending deflection of blade as well as casing deformation during rubbing. The effects of blade physical dimensions, casing stiffness, penetration depths and rotating speeds were analysed by both simulation and experiment which used acceleration sensors to obtain the displacements. It was concluded that when the casing stiffness is greater than the blade stiffness, the rubbing force has a nonlinear characteristic relative to the penetration depth and under this condition blade deformation dominated the normal rubbing force. When the casing stiffness is less than that of the blade the normal rubbing force was observed to have a linear characteristic relative to the penetration depth.

Pennacchi *et al.* [18] analysed the effects of rotor stator contact on seals using experimental study and a mathematical model. Proximity probes and accelerometers were used in the experimental work for data acquisition. The stator in this study is less stiff than the rotor so as to reproduce what happens in a real system when the shaft-line interferes with labyrinth seals. The results highlighted the characteristics of short arc rubs with regard to non-linearities. Ehehalt *et al.* [19] presented an experimental approach based on a modular kit for rotordynamics experiments to confirm various motion patterns brought about by non-linearity due to the rubbing action between rotor and stator. The experimental results verify most motion patterns from simulation results found in literature. The experiment also validated the theoretical hypothesis that the friction coefficient is the key parameter in determining synchronous motion. Cole *et al.* [20] analysed a multimode rotor bearing system with rotor stator clearance and made use of the rotating frame to predict all possible steady state solutions that involve periodic contact with the stator. A harmonic decomposition with generalised fundamental frequency was used to obtain periodic solutions that involve asynchronous partial contacts. The analytical solutions were also compared with previously published experimental results and showed a good agreement. It was observed that for increased unbalance levels, amplitude of the contact mode vibration increased and the response moved from a bouncing forward whirl to a backward whirl solution. Yu and Muszynska [21, 22] experimentally and analytically investigated rotor full annular rub including synchronous forward and backward precession. Wilkes *et al.* [23] investigated the nature of dry whip and whirl through experimental and numerical methods. Childs and Kumar [24] developed analytic dry friction whip and whirl solutions for a rigid rotor model with two contact points. A large body of research conducted by Jiang [25–28] determined the boundary of different nonlinear phenomena and also reveal the related mechanism. Hong [29] revealed the inherent mechanism for partial rubbing motion transmitting into backward whirl motion.

To this point, we have explored various experimental work and all of them measure the vibration of rotors using proximity probes or accelerometers. There is a number of ways for acquiring vibration data and these can be classified into the so called 'contact' and 'non-contact' procedures [30]. Contact procedures physically attach sensors to the structure under study and are very popular as observed earlier. Contact procedures have the drawback of altering the dynamics of the structure via the addition of mass or stiffness if the structure has low mass or is very flexible; furthermore they are often difficult to apply to moving surfaces. Non-contact methods require no physical contact with the structure under test thus circumventing the additional mass or stiffness problem. Typical examples of these non-contact techniques include the Laser Doppler Vibrometer, Scanning Laser Doppler Vibrometer and high speed video (computer vision) which is of interest to this research work.

Computer vision techniques have been used extensively to extract the dynamic characteristics of models. Yoon *et al.* [31] measured the response of a six story model on a shaking table using consumer grade cameras and a reference accelerometer. The proposed computer vision method showed potential to identify the natural frequencies and mode shapes with reasonable levels of accuracy. Harmanci *et al.* [32] also identified the mode shapes of a shear frame using a high speed camera. Sarrafi and Mao [33] and Sarrafi *et al.* [34] conducted studies on a wind turbine blade using high speed cameras and managed to extract natural frequencies and mode shapes of the wind turbine and also identify the nodal points. Melakhessou *et al.* [35] studied the local contact between a drill string and the oil well, and focused on the bottom hole assembly. A mathematical nonlinear model was developed to simulate the dynamics of the lower part of the drill string which takes into account the impact phenomena. Two cameras located in the same plane were used to measure the radial displacements of the drill string. The results obtained were a good match to the numerical simulation proving the efficacy of image processing in data acquisition. Other authors such as [36–38] also used cameras to capture the dynamics of flexible rotor stator contact systems and the data acquisition system proved to be robust in acquiring the motion of the systems in question. Therefore, computer vision methods, though new to this field, have proven to be effective on relatively flexible structures with large displacements and thus making them applicable to our problem.

In this work, the dynamics of rotor stator contact will be studied. The primary focus is to understand orbits featuring asynchronous partial bouncing motions, which often appear in multiple forms due to different physical causes. To the authors' knowledge, this paper contains the first experimental demonstration that the quasi periodic partial contacting motions due to friction are in fact periodic in the rotating frame for an isotropic system. This experimental validation justifies many modelling and analysis approaches that assume periodic responses in the rotating frame. An experimental rig designed to mimic drill string dynamics with no cutting dynamics is used. It is designed to be highly flexible in order to obtain displacements that are easily visible with low natural frequencies. A simple two degrees of freedom mathematical model is used for comparison with the experimental results and the two appear to show acceptable similarities. Firstly, the experimental setup is described and the mathematical model of the experiment is given. The results of the experiment and the mathematical model are presented in the form of spectral intensity plots, orbit plots which will be viewed in both stationary and rotating frames, and also bifurcation diagrams.

Finally, a brief description of the conclusions of this work is given.

2. Experimental setup and Description

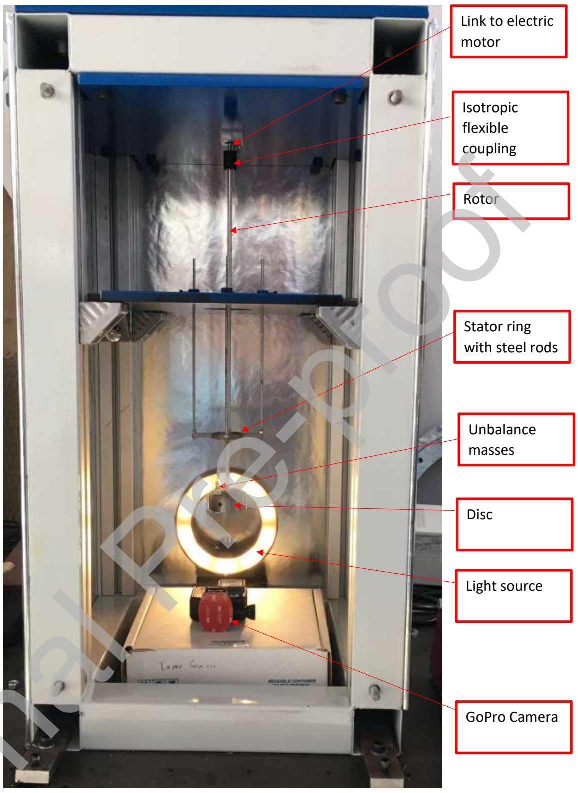

Figure 1: **The components of the experimental rig.**

In this section, the experimental setup that was used in this work, the procedure for data acquisition, and the implementation of the post processing are described. Figure 1 shows the laboratory test rig used in the experimental studies. The rotor test rig consists of a single disc, which has a bolt and nut attached to it to alter the unbalance mass. An isotropic coupling supports the rotor. A concentric stator ring is held in place by steel rods and the stiffness of the stator can be altered by changing the length of the rods. A hammer test is used to obtain the natural frequency of the stator, ω_s which is then be used to calculate the stiffness of the stator, k_s, standard beam theory was used to calculate the analytical stiffness which was found to be in an acceptable range. A brushless electric motor with integrated electronics is located at the top of the rig to give rotational motion to the system. The motor has an embedded system that monitors the rotational speed, although the rotational speed was checked for accuracy using the video measurements. The test rig compartment was enclosed when capturing the videos and therefore a light source was used to enhance the quality of the videos captured by the GoPro camera at 240fps. Based on the Nyquist criterion this therefore means that the sampling rate was enough to extract data for rotational speeds up to 120Hz (7200rpm). For this system the rotational speed will not exceed 600rpm and

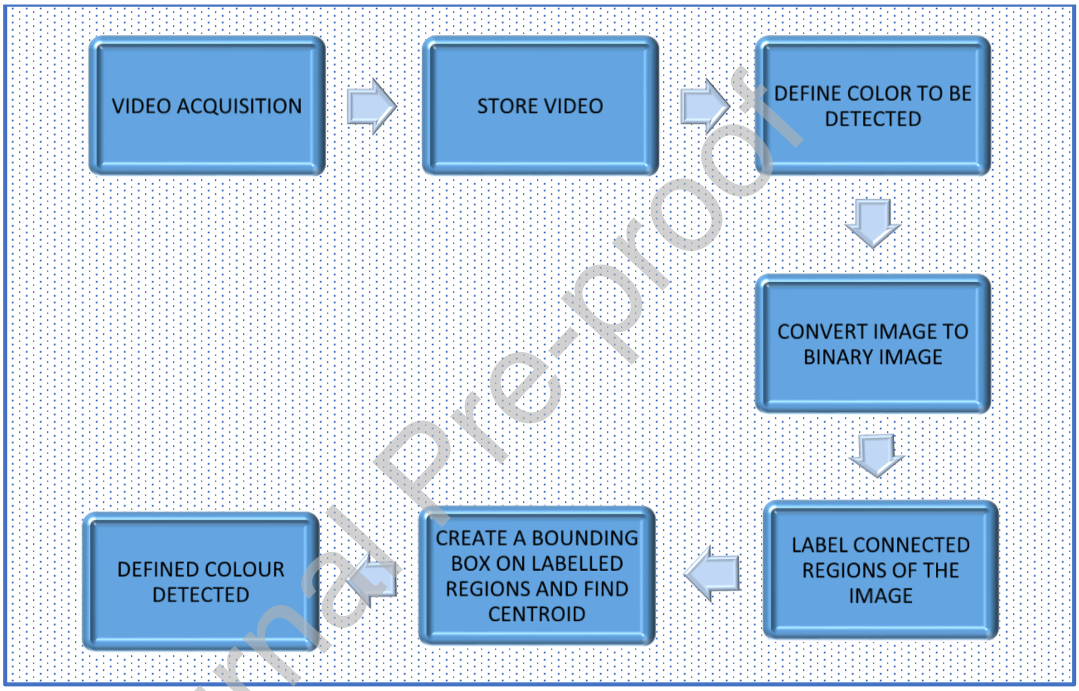

Figure 2: **The flow chart of the algorithm for colour detection.**

therefore any aliasing can be avoided. The response is likely to contain harmonics of the rotor spin speed, and also possible asynchronous response, and hence a significant headroom before the Nyquist frequency is desirable to allow for these uncertainties. Second, we are interested in the rotor orbits, and more points per excitation cycle enable smoother visualisation of the orbits. The frame-rate that was provided by the manufacturer in the camera specification (240fps) was also noted to be inaccurate as compared to the one in the meta-data (239.7277); therefore in this work the frame-rate of the meta-data was used instead of the one specified by the manufacturer.

Figure 2 shows the flow chart of the algorithm for colour detection using MATLAB's Image Processing toolbox. This work makes use of a disk with coloured markers, namely a central green marker, which is used to plot the central position of the disc (orbits), and three red markers, which are used to calculate the rotation angle frame by frame, facilitating accurate conversion from the stationary frame to the rotating frame.

In this work, a GoPro camera was used for video acquisition. A video is a series of images/ frames captured at a particular framerate, and here the frames were captured at approximately 240fps. The video is then post processed frame by frame thus enabling detection and tracking of coloured regions of the image. In their unprocessed form the videos are in RGB format; if the resolution of the image is MxN, the RGB format is a 3D matrix of size MxNx3 where each dimension of the matrix represents red, green and blue colour components of the image.

Firstly, the RGB frame is converted to greyscale format, which is a matrix representation of the intensity of the pixels in an image. This is done to reduce the complexity by converting a 3D image into a 2D image, to ease visualization and also increase the processing speed which could be a hindrance considering the large size or resolutions of the frames. The 24 RGB bits of a pixel are divided equally into three primary colours.

The bits of the required colour, for example green, are subtracted from the greyscale so as to detect the tracked colour. Once the subtraction has been done, a median filter is used to filter out any noise present while maintaining the originality of the image. The filtered image is then converted to binary form representing each frame pixel in the form of zeros and ones so that the output is focused on a particular area of interest. Finally, a bounding box is used to outline the region of the frame where the desired colour is detected. Figure 3 shows the entire process described here and this is just for a single frame. By considering multiple frames the centroid is tracked and Figure 4 shows the tracking of the centroid of a central green marker for a typical bouncing solution.

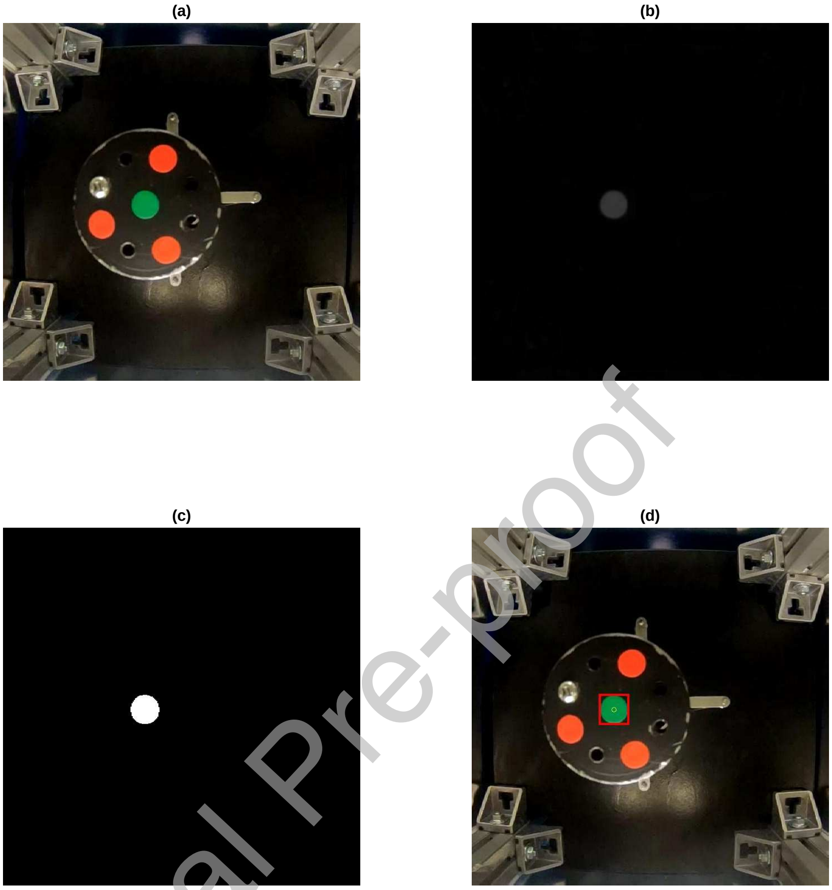

Figure 3: **The image processing technique (a) Original image (b) Filtered image (c) Binary image (d) Detected colour with bounding box and centroid.**

3. Mathematical model

A mathematical model to describe the motion of the rotor was formulated so that comparison with the actual experiment can be made. Figure 5 shows the schematic of the simplified model of the rig. The model used in this study is a lumped parameter model implying that the system is regarded as a mass-spring-damper system whose motion is described by a set of ordinary differential

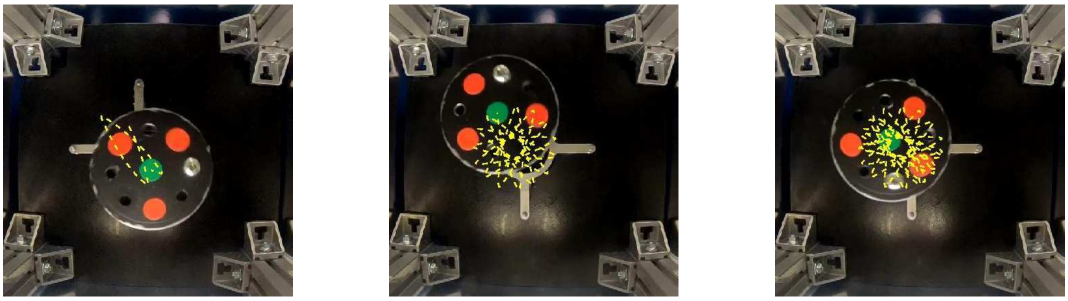

Figure 4: **The tracking of the centroid of the central green marker for a typical bouncing solution.**

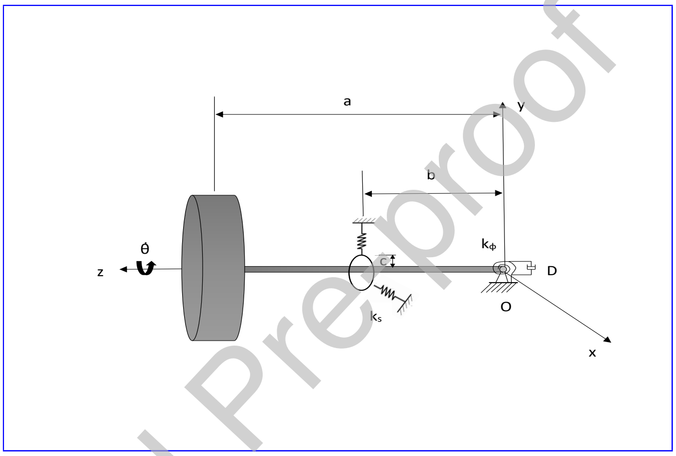

Figure 5: **Schematic of the overhung rotor**

equations(ODEs). The equations are formulated using the Lagrange method and are given by;

$$\begin{cases} J_s\ddot{\phi}_y - J_p\dot{\theta}\dot{\phi}_x + D\dot{\phi}_y + k_\phi\phi_y = am_u e(\dot{\theta}^2\cos\theta + \ddot{\theta}\sin\theta) + M_{\phi_y} \\ J_s\ddot{\phi}_x + J_p\dot{\theta}\dot{\phi}_y + D\dot{\phi}_x + k_\phi\phi_x = am_u e(\ddot{\theta}\sin\theta - \dot{\theta}^2\cos\theta) + M_{\phi_x} \\ M_{\phi_y} = H(||r|| - c^*)k_s\left(-1 + \frac{c}{b\sqrt{\phi_x^2+\phi_y^2}}\right)b^2(\mu\phi_x + \phi_y) \\ M_{\phi_x} = H(||r|| - c^*)k_s\left(1 - \frac{c}{b\sqrt{\phi_x^2+\phi_y^2}}\right)b^2(\mu\phi_y - \phi_x) \end{cases} \tag{1}$$

where ϕ_x and ϕ_y are rotations about the x and y axis, r is the radial displacement of the centre of disc, c is the clearance, $c^* = \frac{ca}{b}$ is the displacement of the centre of the disc that results in contact between rotor and stator, D represents the damping of the system, k_ϕ represents the bearing stiffness , θ is the angle of rotation of the rotor, $\dot{\theta}$ represents the rotor spin speed where $(\,\dot{}\,)$ stands for a time derivative, m_u is the mass unbalance coming from the attached bolt and nuts, e is the eccentricity, J_s is the moment of inertia of the system and is calculated as $J_s = (J_t + a^2 m_d)$, J_t is the transversal moment of inertia and J_p represents the polar moment of inertia and m_d is the disc mass.

$$v_{rel} = \dot{\theta} r_s + \dot{\phi_y}\left(\frac{\phi_x b}{\sqrt{\phi_x^2 + \phi_y^2}}\right) - \dot{\phi_x}\left(\frac{\phi_y b}{\sqrt{\phi_x^2 + \phi_y^2}}\right) \tag{2}$$

Table 1: **Experimental parameters of the test rig. Dimensions are illustrated in Figure 5**

Symbol	Parameter	Value
m_d	mass of disk [kg]	0.22
D_d	Diameter of disk [mm]	45
ω_s	natural frequency of stator [rad/s]	466.4
μ	Coefficient of friction	0.35
h	thickness of disk [mm]	19
w_r	natural frequency of rotor [rad/s]	7.65
a	Disk to coupling length [mm]	400
m_u	Unbalance mass [kg]	0.014
b	Stator to coupling length [mm]	260
r_s	Radius of shaft [mm]	2.5
c	Clearance [mm]	12.5
k_ϕ	Coupling stiffness [Nm/rad]	2
ζ	Damping ratio	0.03

M_{ϕ_x} and M_{ϕ_y} are moments related to the normal force and the tangential force due to friction generated when the system is in contact. μ is the coefficient of friction and can be computed using $\mu = \mu_0 \tanh(v_{rel}/v_0)$, where μ_0 is the maximum friction coefficient and v_0 is a constant and its value can be varied to obtain different friction coefficient profiles in the contact region. v_{rel} is the relative velocity at the contact interface and is calculated as shown in Equation (2). Parameter values for the experimental rig are shown in Table 1. Most of the parameters in this table can be measured in a straight forward way, however, for some of the parameters this is not possible. The natural frequency of the system, ω_r, and the damping ratio, ζ, were obtained by conducting a decay test of a freely swinging rotor using image processing. The stator stiffness, k_s, was also obtained from a hammer test of the stator to give ω_s and then using the equivalent mass to calculate the stiffness. The value of the coefficient of friction, μ, was obtained via a sensitivity analysis to determine which parameter best represented the experimental data obtained.

4. Results and discussion

In this section, the results of both the experiment and the simulation are given in two different subsections and then discussed. Typical results to be discussed include the experimental bifurcation diagram which recreates the numerical brute force bifurcation diagrams, orbits visualised in both stationary and rotating frames, as well as spectral intensity plots, to show how the frequency content of the different solutions changes with the rotor spin speed.

4.1. Experimental Results

Figure 6 shows an experimental bifurcation diagram obtained from the test rig. At each given rotor spin speed, the system is run with an initial perturbation. In many cases the system could take an exceptional amount of time to settle into consistent behaviour; therefore it was left settle for at least ten minutes. At this point, the light source is switched on and the camera is put in place to start the video acquisition. The rig is enclosed and then using the GoPro app which allows for live streaming within the enclosed compartment, the video is captured for 120 seconds. After video acquisition, the image processing technique described in the flow chart of the algorithm in Figure 2 is employed to quantify the dynamics involved. The central green marker is tracked to give the orbits and the time series in both the vertical and horizontal directions. The motion is initially captured in terms of arbitrary image coordinates, and this is converted to millimetres with a scaling factor. The scaling factor is found by having knowledge of the actual dimension of two known points and then finding the corresponding pixel magnitude between these two points, which allows the conversion to be made. The phase space is then sampled using the forcing period. In this way, a single Poincaré return point is obtained for synchronous periodic solutions or multiple return points obtained for both asynchronous bouncing solutions and high amplitude contacting solutions.

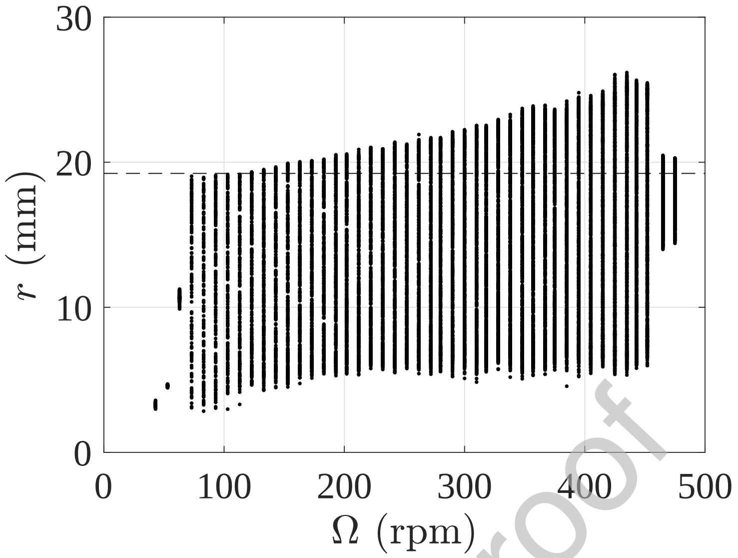

Figure 6: **An experimental bifurcation diagram for a soft stator for ω_s = 465rad/s.**

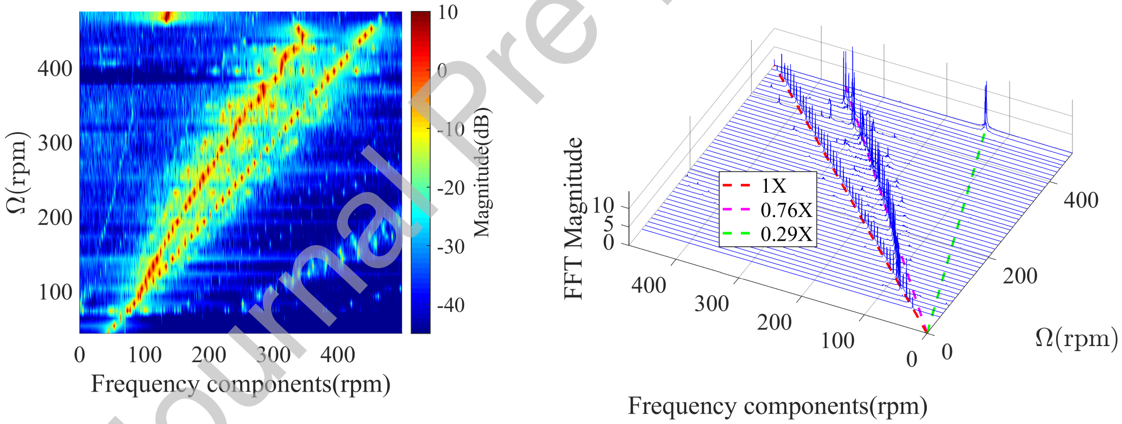

Figure 7: **The experimental spectral intensity plot and the waterfall plot for ω_s = 465rad/s.**

It is evident from the bifurcation diagram in Figure 6 that the first three rotor spin speeds are periodic since a single point is returned. These solutions exhibit this character since all of them are below the first critical speed of the system which is around 72rpm, and they make no contact with the stator therefore the system behaves linearly. These solutions grow as the rotor spin speed is increased because the unbalance forcing is increasing. After the first critical speed the solution then jumps to a solution that is characterised by multiple response levels and as the rotor spin speed increases the intrusion into the flexible stator also increases. The system is then locked into this solution until 453rpm where the solution bifurcates into a high amplitude solution. To get a quick overview of the dynamics of the system the spectral intensity plot and the waterfall plot shown in Figure 7 are obtained which indicates the solution types shown by this system. It therefore evident that there three types of solutions shown by this system, namely the synchronous periodic solution, asynchronous bouncing solution and a high amplitude solution which appears to be backward whirling. The waterfall plot in Figure 7 also shows forcing lines at 1X, 0.76X and 0.29X. The 1X line corresponds to the rotor spin speed. At this point, the origins of the 0.76X line is not yet known but one observation that can be made is that it is only present in asynchronous bouncing type solutions. The waterfall plot shows that there is a line that roughly follows 0.76X particularly towards higher speeds but it is clearly nonlinear, and meets the 1X line near the critical speed therefore; this is mainly used to help illustrate the similarity between simulation and experiment. The 0.29X line is present only in high amplitude solutions where the rotor appears to be backward whirling in the videos. An observation is made that 0.29 is quite close to the ratio of the radius of the rotor to the clearance c which is 0.2, the difference could be due to either the effect of increase response due to stator flexibility or slip in the contact. Therefore the second frequency of these solutions can be approximately predicted by the expression for dry backward whirling velocity $\Omega_{bw} = \dot{\theta}\frac{r_s}{c}$ [39].

To get the full picture of the dynamics at play, the orbits are visualised in both stationary and rotating frames, and the stationary frame FFTs are presented for the three types of solutions. Figure 8 shows orbits and the FFT of a typical synchronous non-contacting solution, the orbit in the stationary frame is circular and when viewed in the rotating frame a single point is observed; this is because in the rotating frame the unbalance force is a static force. The FFT shows a single peak at 63rpm which is the rotor spin speed of this solution.

Figure 9 shows a typical asynchronous bouncing solution at 415 rpm. These solutions appear at approximately 0.76X in Figure 7, and are characterised from their orbits, as shown in Figure 9. The nonlinear rotor response occurs at rotor spin speeds above the first linear critical speed, where the unbalance force is large enough to give a response sufficient to cause rotor-stator contact. The orbit in stationary frame clearly shows the intrusion into the stator whose clearance is represented by the

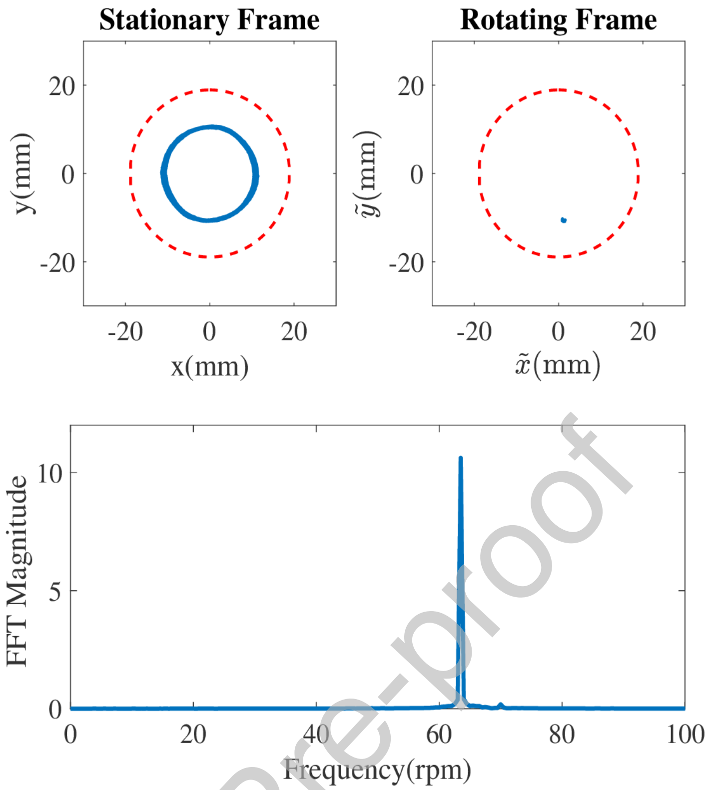

Figure 8: **The experimental orbits of the synchronous periodic solution at 63rpm visualised in the stationary and rotating frames and the corresponding stationary frame FFT.**

red dashed line. The rotating frame orbit shows that the complicated orbit shown in the stationary frame is periodic when viewed in the rotating frame. The stationary frame FFT shows peaks at 415 rpm and 321rpm. The first peak corresponds to the rotor spin speed for this solution and the second one at 321rpm is the contact frequency of the rotor bouncing off the stator. Therefore this solution is an asynchronous periodic bouncing solution and such solutions have also been found via simulation by Cole and Keogh [20, 40]. For large amplitude motion, and assuming instantaneous impact, their analysis [20] for the system considered in this paper gave a potential contacting solution at 356rpm. Although this frequency is significantly higher than the 321rpm measured frequency, the contact is clearly not instantaneous; the finite contact time will stiffen the response and reduce the damping, both of which reduce the calculated frequency of the bouncing solution. This work is therefore

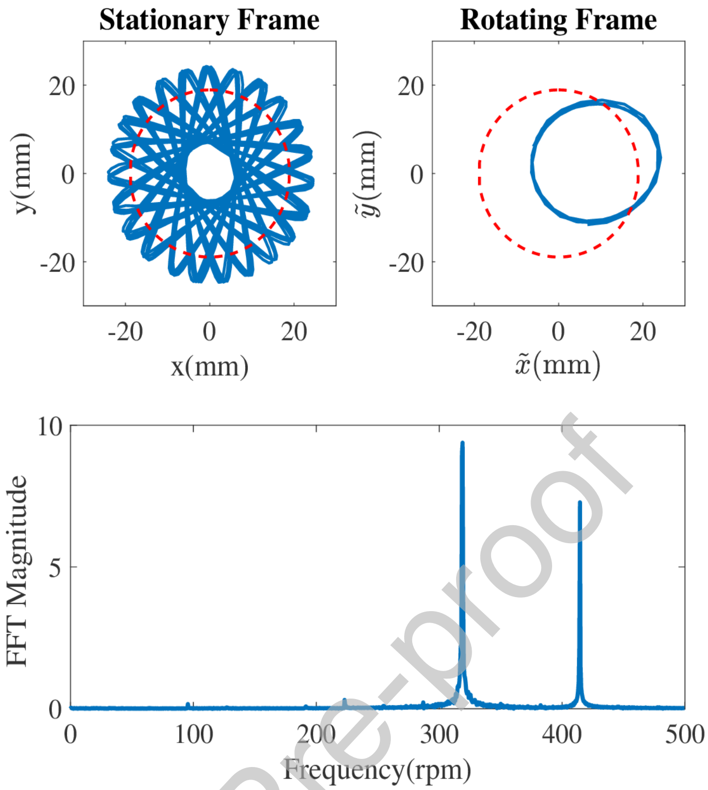

Figure 9: **The experimental orbits of the asynchronous periodic bouncing solution at 415rpm visualised in the stationary and rotating frames with the corresponding stationary frame FFT.**

experimental validation of the existence of such solutions in reality.

Figure 10 shows the final type of solution exhibited by this system at 465rpm. This solution is a high amplitude solution which appears to be a predominantly backward whirling type solution with intermittent stator contact. The orbits visualised in both the stationary and rotating frames are shown. The stationary frame FFT of the solution shows peaks at 465rpm and 134rpm. The 465rpm peak clearly corresponds to the rotor spin speed and the 134rpm peak appears to correspond to the backward whirling(BW) frequency which appears to be dominating the response. A theoretical BW will be permanently attached to the stator which is not the case here. At 465rpm, this BW solution is at a point of transition from asynchronous bouncing motion to a BW solution, and thus it appears to have intermittent contact. At higher rotor spin speeds this solution becomes more in

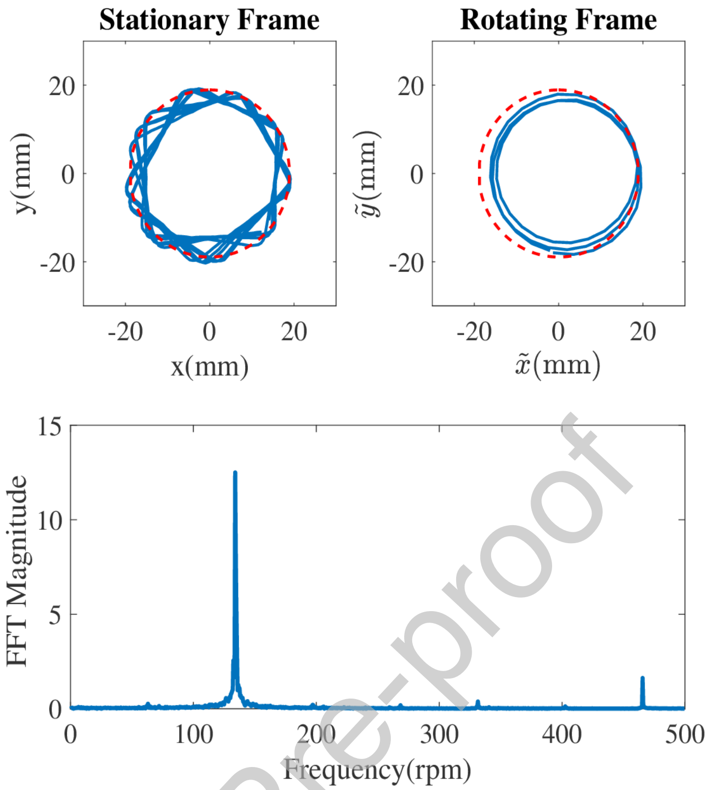

Figure 10: **The experimental orbits of a linear backward whirling solution at 465rpm visualised in the stationary and rotating frames with the corresponding stationary frame FFT.**

contact with the stator and becomes a full BW solution. Because this BW type solution can neither be classified as linear nor dry friction backward whirl (which assumes that the surfaces are locked which is not the case here), the BW solution seen here is termed a quasi dry friction backward whirl (QDFBW). The fact that contact is not constant explains that the whirling speed does not exactly match the theoretical dry backward whirl speed, which assumes non-sliding contact. However, this is a motion that is clearly driven by highly frictional contacts.

4.2. Experimental Run-up and Run-down

Figures 11 and 12 shows spectral intensity plots and waterfall plots for the run-up and the run-down using a stiffer stator at ω_s =628rad/s. To obtain the run-up results, the rig is run for the first speed and then moved slowly to higher speeds without restarting or disturbing the system;

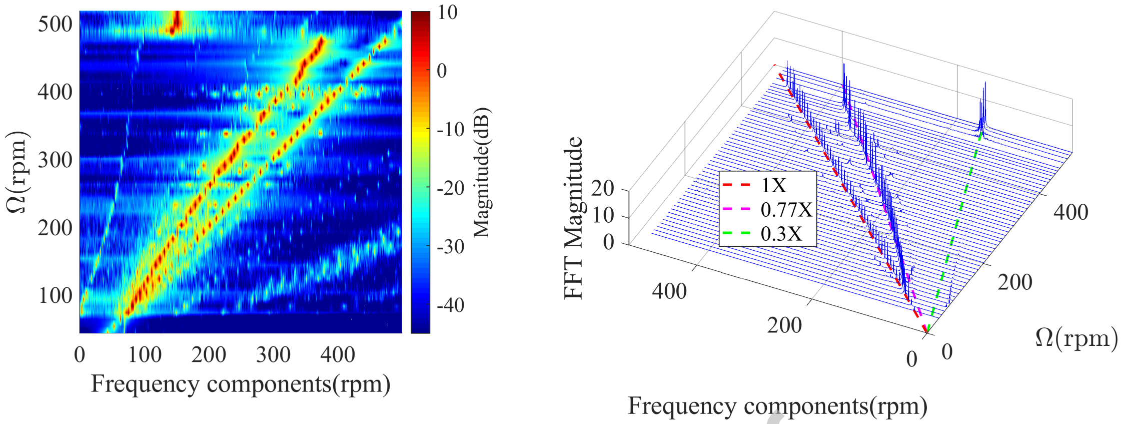

Figure 11: **The experimental spectral intensity plot and waterfall plot for stiff stator at ω_s = 628rad/s for the run-up.**

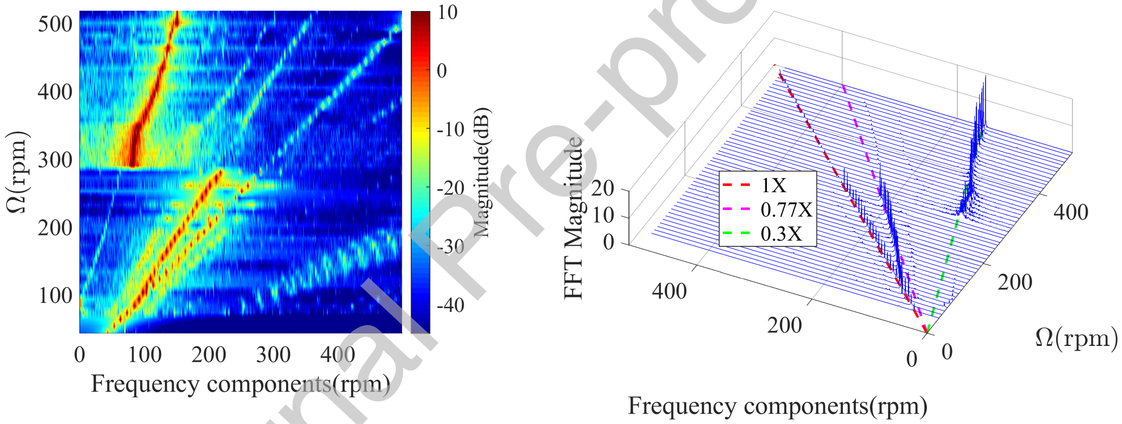

Figure 12: **The experimental spectral intensity plot and waterfall plot for ω_s = 628rad/s for the run-down.**

this therefore means that the final state of the previous rotor spin speed is the initial condition of the preceding speed. The run-down is also implemented in a similar fashion except that this time one has to start with the highest speed of choice and move down to the lowest. For the run-up, it was observed that the QDFBW solutions now started to appear later from 474rpm for the run-up as opposed to 453rpm for the softer stator. The reason for this difference could be that for a softer stator the contact time is greater than that of the stiffer stator therefore this allows for frictional effects to kick in earlier for the softer stator since the QDFBW solution is mainly excited by friction. The location of the forcing lines are observed at 0.3X, 0.77X and 1X. Figure 12 shows the spectral intensity plot and waterfall plots for the run-down for the stiffer stator. It is evident from the plots here that the QDFBW solution branch was tracked from 518rpm to 290rpm after which the asynchronous bouncing solution dominates until the first critical speed, after which the periodic solutions are obtained. The solutions obtained here demonstrated a fundamental property of nonlinear systems which is that of the coexistence of solutions for a given rotor spin speed. We see that QDFBW and asynchronous bouncing solutions can coexist at supercritical rotor spin speeds.

4.3. Simulation Results

In this section the simulated results from the model presented in Section 4.2 are compared with the experimental results and discussed. A schematic of the mathematical model is shown in Figure

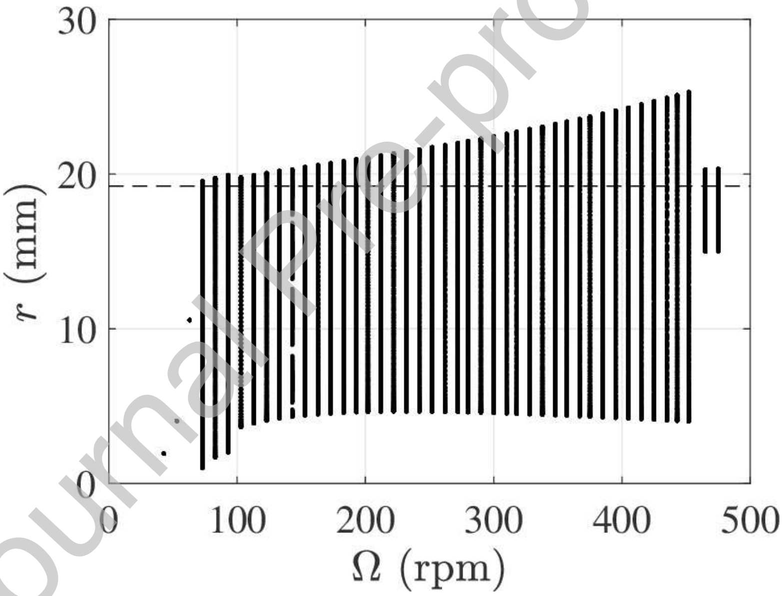

Figure 13: **The simulated bifurcation diagram for a soft stator for $\omega_s = 465$rad/s.**

5. The equations of motion used are shown in Equations (1). The parameters in Table 1 are used in the model. The bifurcation diagram is shown in Figure 13. Figure 14 shows the comparison between experimental and numerical data; only the minimum and maximum response levels are shown. For a given rotor spin speed, a randomized initial condition is created. The equations of

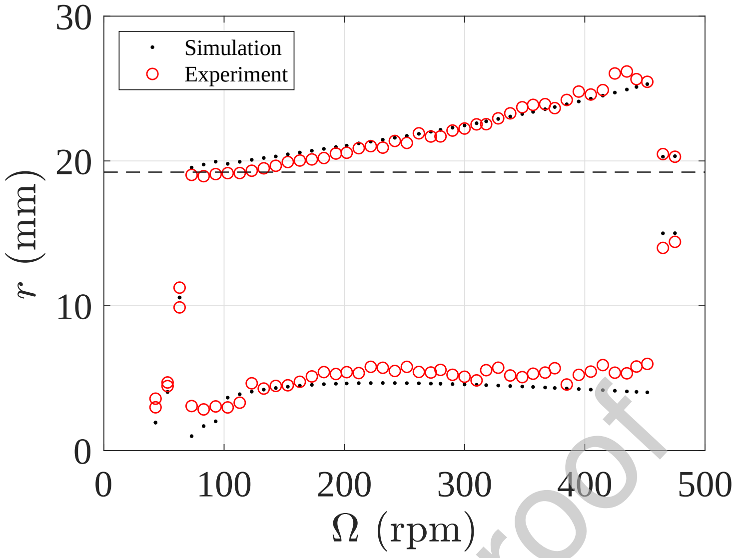

Figure 14: Experimental results superimposed on numerical data.

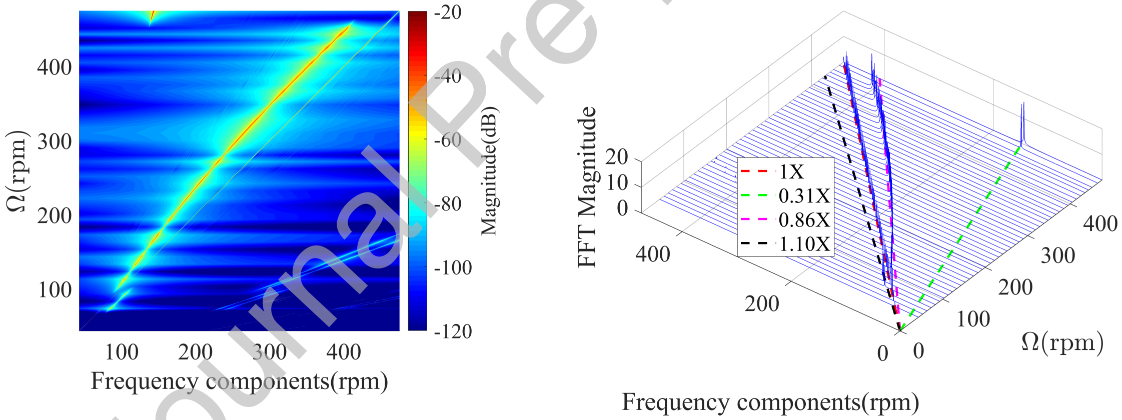

Figure 15: **The simulated spectral intensity plot and waterfall plot for ω_s = 465rad/s.**

motion were numerically integrated using ODE45 with an event detection that detects when the system is in contact so that the integration step size is decreased for accuracy. This is because the system of differential equations becomes stiff when it is in contact. The simulation for each value of rotor spin speed was run for 1000 cycles to ensure that the system has settled and then the last 100

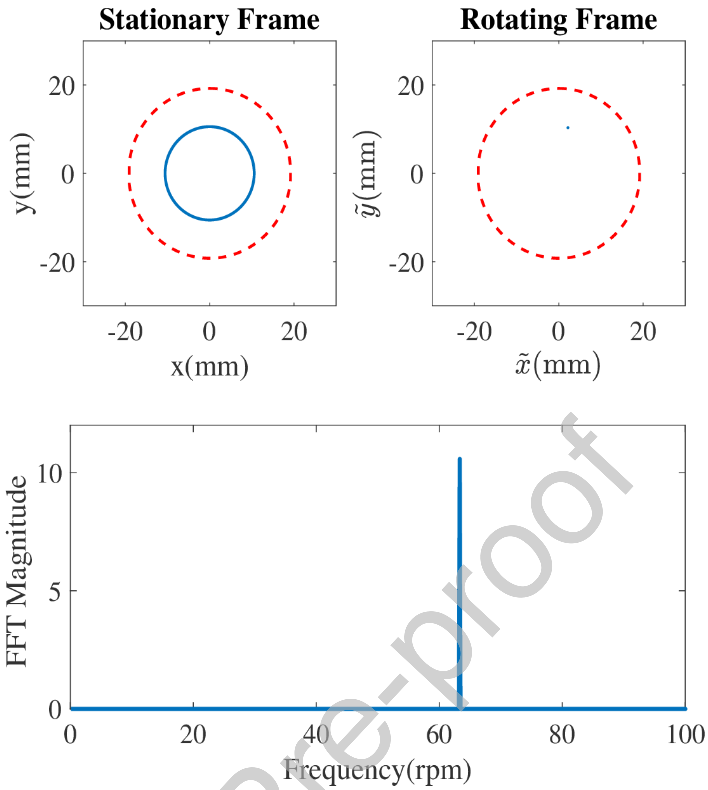

Figure 16: **The simulated orbits of the synchronous periodic solution at 63rpm visualised in the stationary and rotating frames and the corresponding stationary frame FFT.**

cycles are sampled to give the steady state. The phase space in the steady state is then sampled every forcing period and if single point is returned then we have periodic motion but if multiple points are returned then multi-periodic motion is occurring. A comparison of the experimental bifurcation and the simulated bifurcation diagram shows that there is good agreement between the two. There is clearly three classes of solutions available, namely synchronous periodic solutions, asynchronous bouncing solutions as well as high amplitude solutions.

Figure 15 shows the spectral intensity plot and waterfall plot of the simulated bifurcation diagram and clearly when compared with its corresponding experimental plot in Figure 7 the qualitative nature of the solutions are similar. The forcing lines are now at 0.31X, 0.86X, 1X and 1.10X. The 1X line is the rotor spin speed, the 1.10X frequencies only exist for a couple of speeds just after the

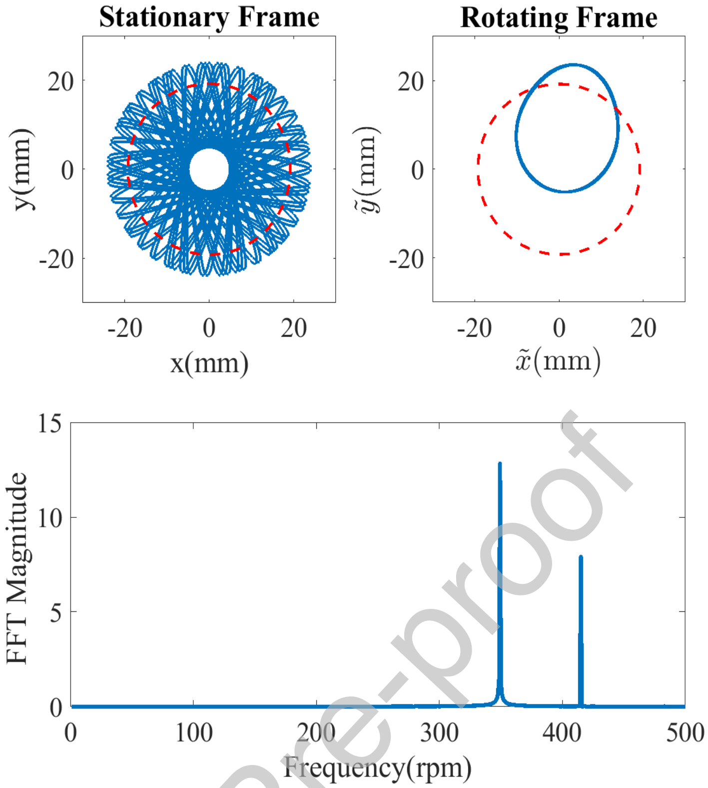

Figure 17: **The simulated orbits of the asynchronous periodic bouncing solution at 415rpm visualised in the stationary and rotating frames with the corresponding stationary frame FFT.**

first critical speed in the resonance expansion region and these solutions are of the asynchronous bouncing type. The 0.86X frequencies dominates most of the bouncing solutions and this is a close match to the 0.76X forcing line in the corresponding experimental waterfall plot. The 0.31X forcing line is a close match to the 0.29X line in the corresponding experimental plot which appeared to be QDFBW solutions. As the experimental results, the orbits are visualised in the stationary and rotating frames, as well as the stationary frame FFT, for speeds corresponding to those presented for the experiment are also plotted here for comparison.

Figure 16 shows the orbits visualised in the stationary and rotating frames at 63rpm. These plots are a good match to the experimental plots shown in Figure 8. The stationary frame orbit is circular, and the rotating frame shows a single point which is consistent with periodic solutions

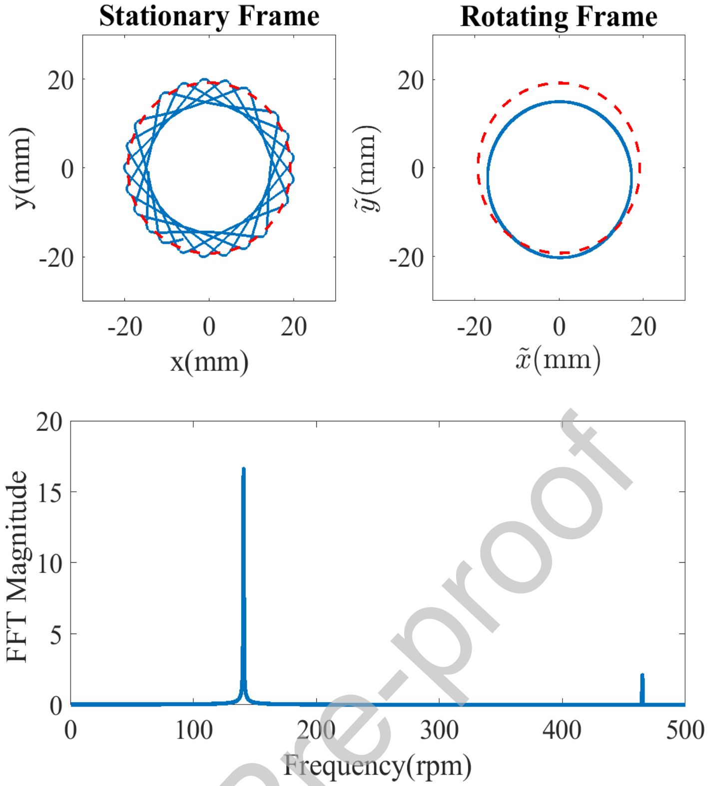

Figure 18: **The simulated orbits of a backward whirling solution at 465rpm visualised in the stationary and rotating frame with the corresponding stationary frame FFT.**

viewed in the rotating frame where the harmonic forcing due to unbalance is static. The stationary frame FFT shows a single peak at 63rpm as expected.

Figure 17 shows the simulated plots corresponding to the experimental asynchronous periodic bouncing solution shown in Figure 9. Similar to the experimental result, a complicated orbit is observed in the stationary frame with a similar intrusion of the stator. In the rotating frame, just like the experimental orbit, the solution appears periodic. The stationary frame FFT shows two peaks which correspond to the rotor spin speed peak and the contact frequency of the rotor bouncing off the stator. These two peaks are at 415rpm and 349rpm; the contact frequency at 349rpm corresponds with the experimental frequency at 321rpm. Figure 18 shows the simulated orbits at 465rpm corresponding to those shown in Figure 10. This was observed to be a QDFBW

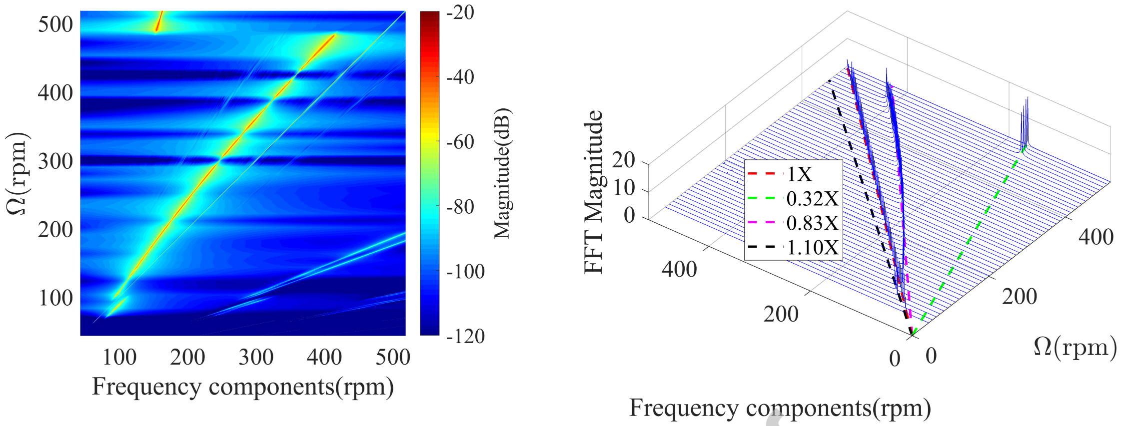

Figure 19: **The simulated spectral intensity plot and waterfall plot for the stiff stator with $\omega_s =$ 628rad/s for the run-up.**

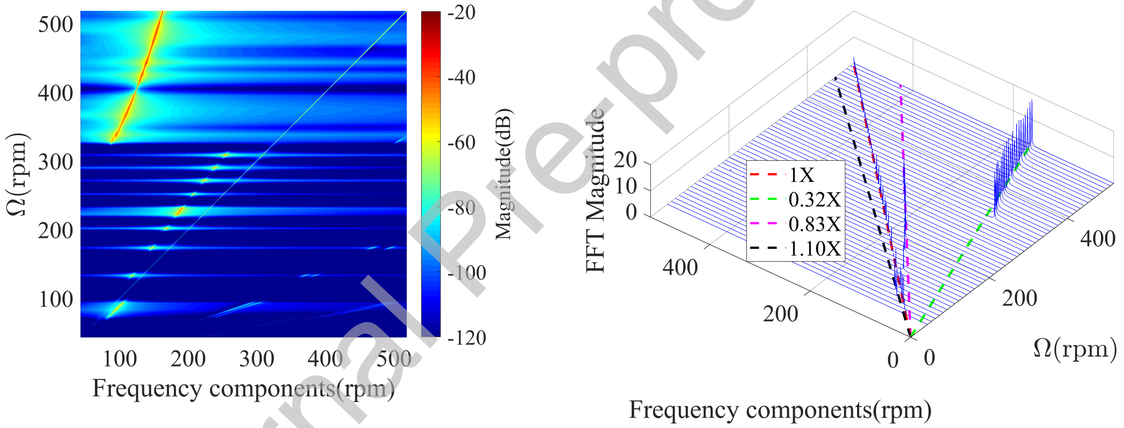

Figure 20: **The simulated spectral intensity plot and waterfall plot for the stiff stator with $\omega_s =$ 628rad/s for the run-down.**

solution. The simulated orbits shown here in both stationary and rotating frames are a good match to their corresponding experimental ones. The simulated stationary frame FFT shows peaks at 465rpm and 140rpm which compare to the experimental ones obtained at 465rpm and 134rpm, which is a good match.

4.4. Simulated Run-up and Run-down

Figures 19 and 20 shows spectral intensity plots and waterfall plots for a stiffer stator at ω_s = 628rad/s. These two plots are qualitatively a good match to the corresponding experimental run-up and run-down results shown in Figures 11 and 12. They clearly demonstrate a fundamental feature of nonlinear systems which is that solutions can coexist and are highly dependent on initial conditions.

5. Conclusions

This paper has presented a rotor-stator contact experiment that was validated using simulated results of a two degree of freedom model. Bifurcation diagrams, spectral intensity plots, orbit plots visualised in both stationary and rotating frame were used to classify the different solutions. The data acquisition in the experiment was conducted using an image processing technique by making use of the image processing toolbox in MATLAB. For the simulation, numerical integration was used and the results compared with the experimental data for validation. The good agreement between results and experiments confirms the effectiveness of this image processing technique and that consumer grade cameras like GoPro can be effective in capturing dynamics of structures. In the simulation, the Coulomb friction model was used and the qualitative agreement between experimental and simulated results shows that for these problems this model can capture the dynamics of this system very well. In the experiment, asynchronous periodic bouncing solutions were observed. These were previously reported in other work but not confirmed experimentally. These asynchronous periodic bouncing solutions appear to be quite complicated and aperiodic in the stationary frame but when viewed in the rotating frame they appear to be simple and periodic. In the high rotor spin speed range of the system quasi dry friction backward whirl solutions were observed. These were excited by the presence of friction in the system. For a softer stator, it was observed that the quasi dry friction backward whirl solutions appeared at lower rotor spin speeds than for a stiffer stator. It was observed that the reason for this is that for a softer stator the contact time duration was higher than that of a stiffer stator therefore frictional effects kick in earlier than for high stiffness where the contact time is lower.

Acknowledgements

The research leading to these results has received funding from Swansea University via the ZCCE PhD scholarship.

References

[1] M. Kanzari, I. Shahin, M. Alqaradawi, B. Balachandran, Drill string nonlinear vibrations: experimental studies and finite-element analysis, in: Journal of Physics: Conference Series, volume 1075, IOP Publishing, 2018, p. 012010.

[2] D. R. H. Stroud, L. A. Lines, D. J. Minett-smith, et al., Analytical and experimental backward whirl simulations for rotary steerable bottom hole assemblies, in: SPE/IADC Drilling Conference and Exhibition, Society of Petroleum Engineers, 2011.

[3] H. Ma, F. Yin, Y. Guo, X. Tai, B. Wen, A review on dynamic characteristics of bladecasing rubbing, Nonlinear Dynamics 84 (2016) 437–472.

[4] E. Chipato, A. Shaw, M. Friswell, Effect of gravity-induced asymmetry on the nonlinear vibration of an overhung rotor, Communications in Nonlinear Science and Numerical Simulation 62 (2018) 78–89.

[5] A. Shaw, A. Champneys, M. Friswell, Asynchronous partial contact motion due to internal resonance in multiple degree-of-freedom rotordynamics, in: Proc. R. Soc. A, volume 472, The Royal Society, 2016.

[6] A. D. Shaw, A. R. Champneys, M. I. Friswell, Normal form analysis of bouncing cycles in isotropic rotor stator contact problems, International Journal of Mechanical Sciences 155 (2019) 83–97.

[7] A. Zilli, R. J. Williams, D. J. Ewins, Nonlinear dynamics of a simplified model of an overhung rotor subjected to intermittent annular rubs, Journal of Engineering for Gas Turbines and Power 137 (2015) 065001.

[8] E. Chipato, A. Shaw, M. Friswell, Frictional effects on the nonlinear dynamics of an overhung rotor, Communications in Nonlinear Science and Numerical Simulation (2019).

[9] H. Ma, Q. Zhao, X. Zhao, Q. Han, B. Wen, Dynamic characteristics analysis of a rotorstator system under different rubbing forms 39 (2015) 2392–2408.

[10] H. Ma, Y. Lu, Z. Wu, X. Tai, B. Wen, Vibration response analysis of a rotational shaftdiskblade system with blade-tip rubbing 107 (2016) 110–125.

[11] M. Torkhani, L. May, P. Voinis, Light, medium and heavy partial rubs during speed transients of rotating machines: Numerical simulation and experimental observation, Mechanical Systems and Signal Processing 29 (2012) 45–66.

[12] H. Ma, C. Shi, Q. Han, B. Wen, Fixed-point rubbing fault characteristic analysis of a rotor system based on contact theory, Mechanical Systems and Signal Processing 38 (2013) 137–153.

[13] F. Chu, W. Lu, Experimental observation of nonlinear vibrations in a rub-impact rotor system, Journal of Sound Vibration 283 (2005) 621–643.

[14] C. Wang, D. Zhang, Y. Ma, Z. Liang, J. Hong, Theoretical and experimental investigation on the sudden unbalance and rub-impact in rotor system caused by blade off, Mechanical Systems and Signal Processing 76-77 (2016) 111–135.

[15] G. Chen, Simulation of casing vibration resulting from blade-casing rubbing and its verifications, Journal of Sound Vibration 361 (2016) 190–209.

[16] H. Ma, F. Yin, Z. Wu, X. Tai, B. Wen, Nonlinear vibration response analysis of a rotor-blade system with blade-tip rubbing, Nonlinear Dynamics 84 (2016) 1225.

[17] H. Ma, X. Tai, Q. Han, Z. Wu, D. Wang, B. Wen, A revised model for rubbing between rotating blade and elastic casing, Journal of Sound Vibration 337 (2015) 301–320.

[18] P. Pennacchi, N. Bachschmid, E. Tanzi, Light and short arc rubs in rotating machines: Experimental tests and modelling, Mechanical Systems and Signal Processing 23 (2009) 2205–2227.

[19] U. Ehehalt, O. Alber, R. Markert, G. Wegener, Experimental observations on rotor-to-stator contact, Journal of Sound Vibration 446 (2019) 453–467.

[20] M. Cole, P. Keogh, Asynchronous periodic contact modes for rotor vibration within an annular clearance, Proceedings of the Institution of Mechanical Engineers, Part C: Journal of Mechanical Engineering Science 217 (2003) 1101–1115.

[21] J. J. Yu, P. Goldman, D. E. Bently, A. Muzynska, Rotor/seal experimental and analytical study on full annular rub 124 (2002) 340–350.

[22] A. Muszynska, Rotordynamics, New York: Taylor & Francis, 2005. doi:`10.1201/9781420027792`.

[23] J. C. Wilkes, D. W. Childs, B. J. Dyck, S. G. Phillips, The numerical and experimental characteristics of multimode dry-friction whip and whirl 132 (2010).

[24] D. W. Childs, D. Kumar, Dry-friction whip and whirl predictions for a rotor-stator model with rubbing contact at two locations 134 (2012).

[25] J. Jiang, H. Ulbrich, The physical reason and the analytical condition for the onset of dry whip in rotor-to-stator contact systems 127 (2005) 594–603.

[26] J. Jiang, The analytical solution and the existence condition of dry friction backward whirl in rotor-to-stator contact systems 129 (2007) 260–264.

[27] J. Jiang, Determination of the global responses characteristics ofapiecewise smooth dynamical system with contact 57 (2009) 351–361.

[28] J. Jiang, Z. Wu, Determining the characteristics of a self-excited oscillation in rotor/stator systems from the interaction of linear and nonlinear normal modes, Int. J. Bifurc. Chaos 20 (2010) 4137–4150.

[29] J. Hong, P. Yu, D. Zhang, Y. Ma, Nonlinear dynamic analysis using the complex nonlinear modes for a rotor system with an additional constraint due to rub-impact 116 (2019) 443–461.

[30] A. Shaw, S. Neild, D. Wagg, P. Weaver, Single source three dimensional capture of full field plate vibrations, Experimental Mechanics 52 (2012) 965 974.

[31] H. Yoon, H. Elanwar, H. Choi, M. GolparvarFard, B. F. Spencer, Targetfree approach for visionbased structural system identification using consumergrade cameras, Struct. Control Health Monit 23 (2016) 14051416.

[32] E. Harmanci, Y, Z. Lai, U. Gulan, M. Holzner, E. Chatzi, Computer vision aided structural identification: Feature tracking using particle tracking velocimetry versus optical flow, in: 5th International Electronic Conference on Sensors and Applications, volume 4(33), 2019.

[33] A. Sarrafi, Z. Mao, Using 2d phase-based motion estimation and video magnification for binary damage identification on a wind turbine blade, in: Model Validation and Uncertainty Quantification, Volume 3, Springer, 2019. URL: `http://dx.doi.org/10.1007/978-3-319-74793-4_19`. doi:`10.1007/978-3-319-74793-4_19`.

[34] A. Sarrafi, P. Poozesh, C. Niezrecki, Z. Mao, Detection of natural frequency and mode shape correspondence using phase-based video magnification in large-scale structures, in: Structural Health Monitoring, Photogrammetry & DIC, Volume 6, Springer, 2019. URL: `http://dx.doi.org/10.1007/978-3-319-74476-6_12`. doi:`10.1007/978-3-319-74476-6_12`.

[35] H. Melakhessou, A. Berlioz, G. Ferraris, A nonlinear well-drillstring interaction model, J. Vib. Acoust. 125 (2003) 46–52.

[36] C.-M. Liao, N. Vlajic, H. Karki, B. Balachandran, Parametric studies on drill-string motions, International Journal of Mechanical Sciences 54 (2012) 260–268.

[37] N. A. Vlajic, Dynamics of slender, flexible structures, Ph.D. thesis, 2014.

[38] C.-M. Liao, Experimental and numerical studies of drill-string dynamics, Ph.D. thesis, 2011.

[39] O. Alber, R. Markert, Rotor-stator contact overview of current research 16 (2014) 03001.

[40] M. O. Cole, On stability of rotordynamic systems with rotor–stator contact interaction, Proceedings of the Royal Society A: Mathematical, Physical and Engineering Sciences 464 (2008) 3353–3375.

Credit Author Statement

Elijah Tapiwa Chipato: Simulation, Development of Experimental Rig, Writing- Reviewing and Editing

Michael I Friswell and Alexander D Shaw: Reviewing and Editing

Rafael Sanchez Crespo: Development of Experimental Rig

Declaration of interests

The authors declare that they have no known competing financial interests or personal relationships that could have appeared to influence the work reported in this paper.